ADVANCED MATERIALS

Supporting Information

Thickness-Dependent Elastic Softening of Few-Layer Free-Standing MoSe$_2$

Visnja Babacic, David Saleta Reig, Sebin Varghese, Thomas Vasileiadis, Emerson Coy, Klaas-Jan Tielrooij, and Bartlomiej Graczykowski*

"Thickness-dependent Elastic Softening of Few-layer Free-standing MoSe₂"

Visnja Babacic[1], David Saleta Reig[2], Sebin Varghese[2], Thomas Vasileiadis[1], Emerson Coy[3], Klaas-Jan Tielrooij[2] and Bartlomiej Graczykowski[1,4]

[1] *Faculty of Physics, Adam Mickiewicz University, Uniwersytetu Poznanskiego 2, 61-614 Poznan, Poland*
[2] *Catalan Institute of Nanoscience and Nanotechnology (ICN2), CSIC and BIST, Campus UAB, Bellaterra, 08193, Barcelona, Spain*
[3] *NanoBioMedical Centre, Adam Mickiewicz University, Wszechnicy Piastowskiej 3, 61-614, Poznan, Poland*
[4] *Max Planck Institute for Polymer Research, Ackermannweg 10, 55128, Mainz, Germany. Email Address: graczykowski@mpip-mainz.mpg.de*
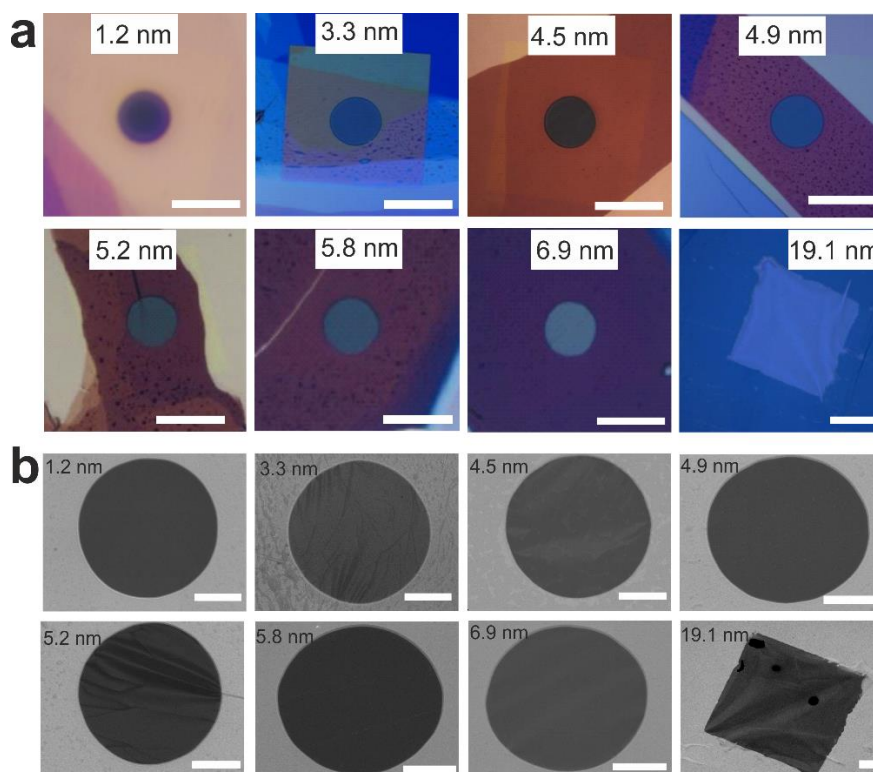
Section S1. MoSe₂ membranes

Figure S1. (a) Optical and (b) scanning electron microscopy images of MoSe₂ membranes of different thickness (indicated in the figure). Scale bars in (a) and (b) are 20 μm and 5 μm, respectively.

We exfoliated MoSe₂ flakes onto PDMS [Fig. S2 (a – e)] and, prior to dry transfer, we estimated the flake thickness from transmission optical images. We obtained these using a Nikon microscope set for Köhler illumination and analyzed the images with ImageJ software. First, we split the image into RGB color channels and took the green channel intensity profiles across the regions of interest. This allowed us to quantify the intensity drop with respect to the substrate caused by a flake with a given thickness. Two terraced flakes [Fig. S2 (a, b)] (not transferred or studied by BLS) with known thickness values allowed us to qualitatively sort our samples by
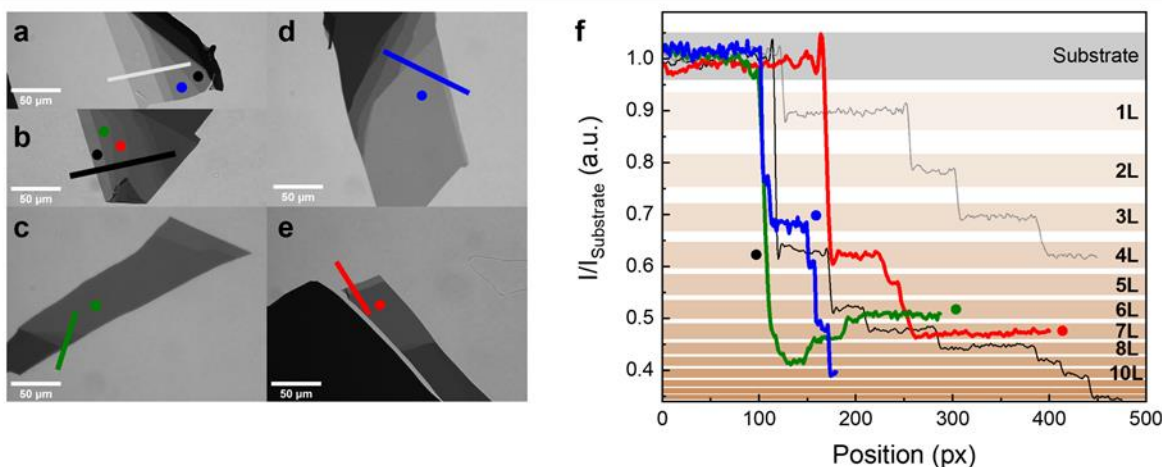
Figure S2. Thickness estimation from optical contrast. (a – e) Green channel transmission images of MoSe$_2$ flakes on PDMS, prior to dry transfer: (a) Calibration Sample A, measured both with photoluminescence and optical contrast. b) Calibration Sample B, with thicknesses measured both with photoluminescence and AFM. (c-e). Exemplary flakes that we later transferred onto holey substrates and studied in this work with BLS. (f) Optical contrast measurements for the samples in panels a-e.

number of layers. The thicknesses of the flakes used for calibrating optical contrast measurements were confirmed with photoluminescence (PL) measurements (Fig. S3). This allowed us to unambiguously assign thicknesses to 1L, 2L, and 3L, which are all in excellent agreement with our results from optical contrast, as we show in Figs. S2 and S3. Furthermore, the PL peak position of 1.57 eV for monolayer MoSe$_2$ is in excellent agreement with results in the literature.[1]
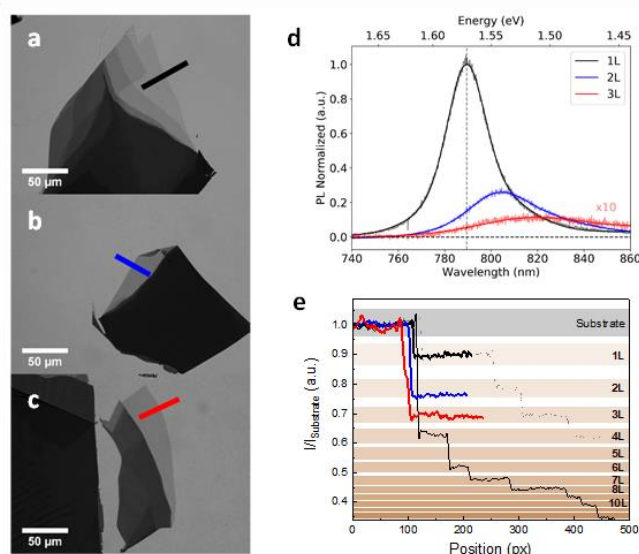

Figure S3. (a-c) Calibration Samples C, D and E, whose thicknesses are determined through (d) photoluminescence and (e) optical contrast measurements.

Finally, we normalized the intensity profiles by the average intensity of a significant area of the corresponding substrate for comparison with the flakes of known thickness. The thicknesses of $MoSe_2$ membranes obtained in this way are gathered in Table S1

Atomic Force Micrographs reported in Fig. S4, show the thickness at the step-like border region of the $MoSe_2$ flakes (Table S1). However, we observe discrepancies with thicknesses measured by optical method for samples with thicknesses below 8L. The optical contrast technique is very accurate for relatively thin samples, <9L, while AFM measurements are more accurate for thicknesses >8L. These discrepancies can be attributed to the higher susceptibility of AFM measurement to polymeric residues, i.e., from the sample preparation process and the non-ideal interface between $MoSe_2$ and the support. The combination of AFM and optical contrast allows the thickness identification of the $MoSe_2$ membranes. AFM image of the freestanding region for the exemplary $MoSe_2$ sample [Fig. S5 (a)] showed sub-nanometer roughness over several microns [Fig. S5 (b)], confirming the absence of small wrinkles on the region investigated by BLS.

Table S1. Thicknesses determined from optical contrast method and AFM.

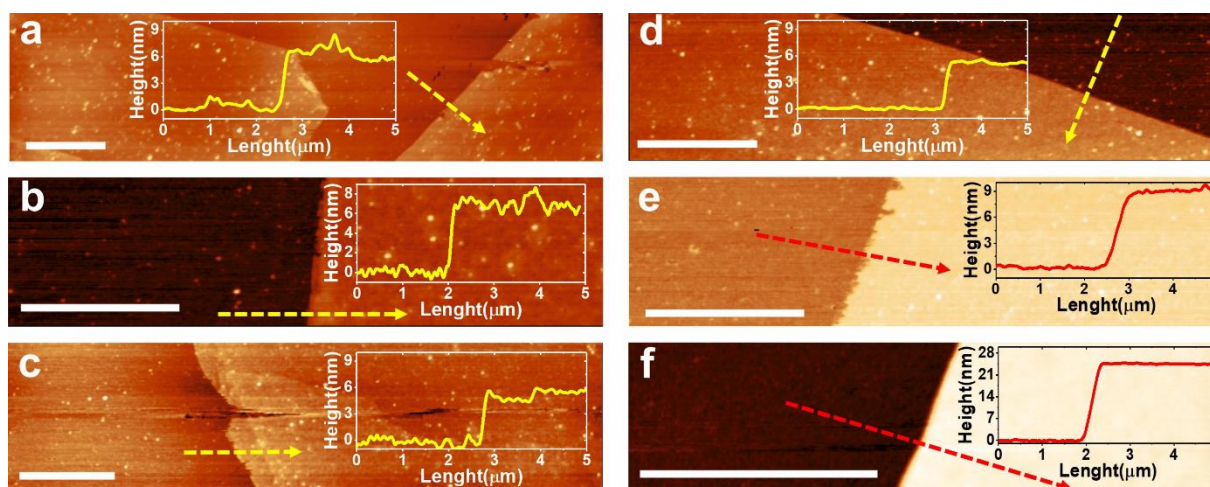| Optical contrast, d (nm)	AFM. d (nm)
1.9 (3L)	NA
2.9±0.4 (4-5L)	6.3±1.9
4.2±0.4 (6-7L)	NA
4.5(7L)	6.7±1.5
5.2(8L)	5.1±1.6
5.5±0.4(8-9L)	5.2±1.2
NA	8.8±0.7
NA	24.7±1.3

Figure S4. Atomic force microscopy images of the step-like edges for $MoSe_2$ samples acquired from the supported region, several tens of microns away from membranes. Dashed arrows show the profile collection area (insets). The micrographs correspond to the thicknesses (a) 6.3±1.9 nm, (b) 6.7±1.5 nm, (c) 5.1±1.6 nm, (d) 5.2±1.2 nm, (e) 8.8±0.7 nm, and (f) 24.7±1.3 nm with the roughness (Rq) as the error of the measurement. Scale bars are 4 µm.
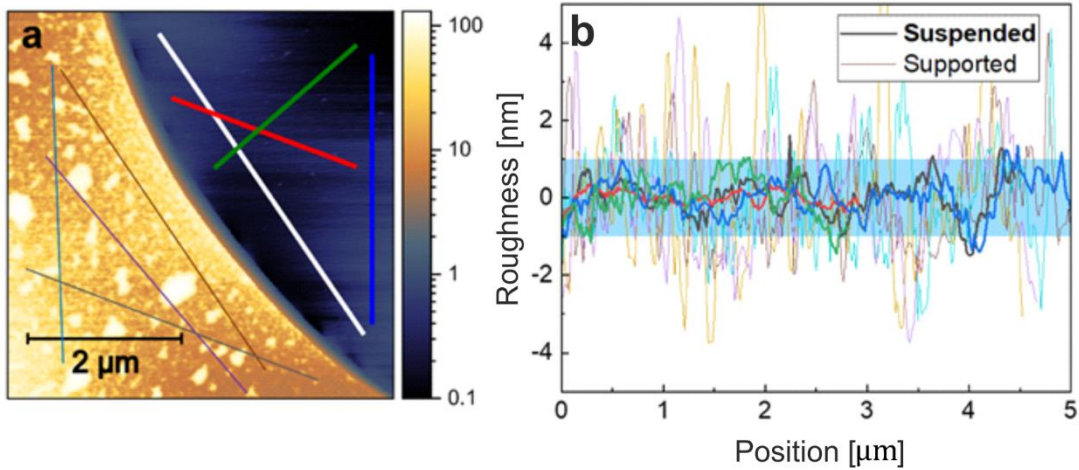
Figure S5. (a) AFM image of the supported and freestanding regions of exemplary MoSe$_2$ sample and (b) corresponding roughness measurements.

Section S2: BLS spectra of different bulk TMDCs – MoSe$_2$, MoTe$_2$ and WS$_2$

To investigate the effect of the high opacity of MoSe$_2$ on the BLS peak corresponding to the longitudinal bulk acoustic wave (L BAW) with wave number $Q = 4\pi n_1/\lambda$, we performed BLS experiments in backscattering geometry extending the free spectral range to 90 GHz. As a reference, we used two other TMDCs, i.e., bulk MoTe$_2$ and WS$_2$. The resulting spectra are displayed in Fig. S6. The sharp peaks in the spectral region from about 27 to 44 GHz correspond to the backscattering BLS from the glass optics used in the experiment. In the spectra of WS$_2$ and MoTe$_2$, we can notice two broad peaks at about 47 and 49 GHz, respectively. These peaks, according to C_{33} from the literature[2][3] can be assigned to L BAWs propagating in the [001] direction. In the case of the MoSe$_2$ the L BAW peak expected at about 51 GHz[4] (indicated by arrow) was not resolved. The broadening of BLS peaks due to medium opacity can be calculated from the formula $\Delta f/f = 2n_2/n_1$[5], n_1 and n_2 stand for the real and imaginary parts of the refrective index. Indeed, as indicated in Fig. S6 the relative width is the highest for MoSe$_2$ explaining the absence of the peak corresponding to the L BAW in the spectra. Strong suppression of the usual backscattering BLS can enable detection of surface-like waves due to so called sub-surface photoelastic mechanism in addition to the surface ripple mechanism. [6–9]
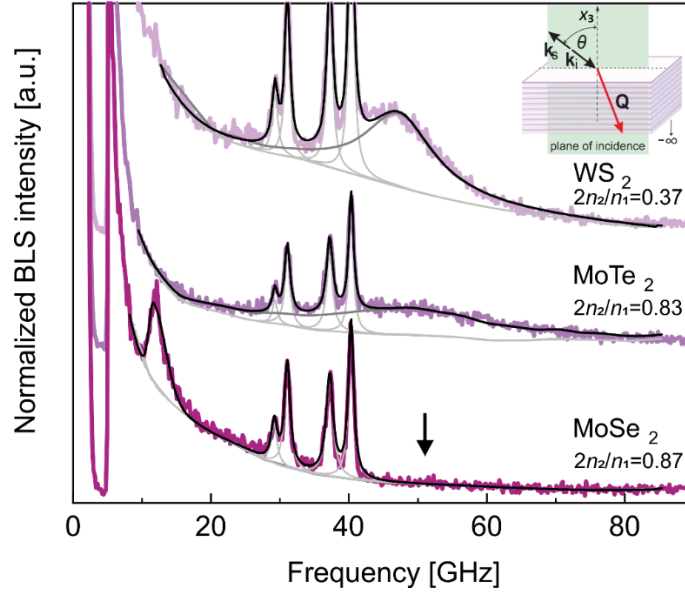
Figure S6. Experimental BLS spectra for bulk MoSe$_2$, MoTe$_2$ and WS$_2$ obtained in the backscattering geometry. The sharp peaks in the region between 27 and 44 GHz correspond to the backscattering BLS from the glass optics. Symbols n_1 and n_2 stand for real and imaginary parts of the refractive index, respectively. Inset shows a schematic illustration of the used BLS geometry where symbols **k$_i$**, **k$_s$**, and **Q** denote incident light, scattered light, and bulk acoustic wave vectors. The incident angle was set to $\theta = 45°$ to avoid detector saturation due to intense back-reflected light.

Section S3. Influence of the elastic constants on the dispersion of RSWs
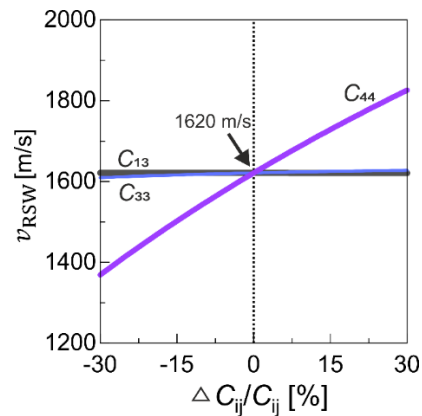

Figure S7. The dependence of RSW velocity, v_{RSW} on the relative change of elastic constants. The black arrow indicates the experimentally determined $v_{\mathrm{RSW}} = 1620$ m/s for which we calculated $C_{44} = 18.8$ GPa.

Section S4. Dispersion relations, BLS spectra and membrane thickness – numerical calculations.

S4.1. Dispersion relation of Lamb waves

The equation of motion for the pre-stressed material is given by the formula:

$$\frac{\partial}{\partial x_j}\left(\sigma_{ij} + \sigma_{jl}^0 \frac{\partial u_i}{\partial x_l}\right) = \rho \frac{\partial^2 u_i}{\partial t^2}, \tag{1}$$

where u_i are the displacement component, ρ is the mass density and σ_{jl}^0 is the Cauchy stress tensor related to the residual biaxial residual stress σ^0, that can be represented as a diagonalized matrix with non-zero components $\sigma_{11} = \sigma_{22} = \sigma^0$.

The strain tensor $u_{ij} = \frac{1}{2}\left(\frac{\partial u_i}{\partial x_j} + \frac{\partial u_j}{\partial x_i}\right)$ and the Cauchy stress tensor σ_{ij} are related by means of Hooke's law: $\sigma_{ij} = C_{ijkl} u_{kl}$, where C_{ijkl} is the elastic tensor. The elastic tensor, C_{ijkl} can be expressed as 6 x 6 matrix in the Voigt notation. For a hexagonal crystal, this matrix has five non-zero, independent elastic constants: $C_{11}, C_{12}, C_{13}, C_{33}, C_{44}$, given as:

$$C_{KL} = \begin{bmatrix} C_{11} & C_{12} & C_{13} & 0 & 0 & 0 \\ C_{12} & C_{11} & C_{13} & 0 & 0 & 0 \\ C_{13} & C_{13} & C_{33} & 0 & 0 & 0 \\ 0 & 0 & 0 & C_{44} & 0 & 0 \\ 0 & 0 & 0 & 0 & C_{44} & 0 \\ 0 & 0 & 0 & 0 & 0 & C_{66} \end{bmatrix}, \text{ where } C_{66} = \frac{1}{2}(C_{11} - C_{12}). \tag{2}$$

We assume the solution of Eq. (1) is a linear combination of three ($i = 1,2,3$) plane waves with amplitudes u_{i0}:

$$u_i = u_{i0} \exp\left[iq(l_j x_j - vt)\right] , \tag{3}$$

where, v denotes the phase velocity. The acoustic wave vector is given by $\mathbf{q} = q(l_1, l_2, l_3)$, where l_i stands for direction cosine. Due to the hexagonal symmetry, the velocities of acoustic waves propagating in (001) do not depend on the direction of propagation (given by l_i). In other words, the (001) plane is elastically isotropic. Thus, for convenience, we set $l_1 = 1$, $l_2 = 0$. From the substitution of Eq. (3) into Eq. (1), we obtain the secular equation, which gives nontrivial solutions for u_i only if:

$$\left|\Gamma_{ij} - \delta_{ij}\rho v^2\right| = 0, \tag{4}$$

where $\Gamma_{ij} = (C_{ijkl} + \delta_{ik}\sigma_{jl}^0)l_j l_l$ denotes the acoustic tensor and δ_{ik} is the Kronecker delta. For any value of v, Eq. (4) has $n = 6$ solutions for $l_3^{(n)}$. Thus, the general solution for u_i is a superposition of six waves:

$$u_i = \sum_n^6 A^{(n)} u_{i0}^{(n)} \exp\left[iq\left(l_3^{(n)} x_3\right)\right] \exp[iq(l_1 x_1 + vt)], \tag{5}$$

where $A^{(n)}$ and $u_{i0}^{(n)}$ are weighting factors and partial wave amplitudes, respectively. We set two stress-free boundary conditions for the upper ($x_3 = 0$) and lower ($x_3 = -d$) surfaces of the membrane:

$$\sigma_{i3}(x_3 = 0) = C_{i3kl} \left. \frac{\partial u_k}{\partial x_l} \right|_{x_3=0} = 0, \tag{6a}$$

$$\sigma_{i3}(x_3 = -d) = C_{i3kl} \left. \frac{\partial u_k}{\partial x_l} \right|_{x_3=-d} = 0. \tag{6b}$$

By substituting Eq. (5) into Eqs. (6a) and (6b) we obtain:

$$\sum_n^6 C_{i3kl} A^{(n)} u_{k0}^{(n)} l_l^{(n)} = 0, \tag{7}$$

$$\sum_n^6 C_{i3kl} A^{(n)} u_{k0}^{(n)} l_l^{(n)} \exp\left[-(iql_3^{(n)}d)\right] = 0. \tag{8}$$

The above is a set of six equations witch can be written in matrix form as a multiplication of the 6×6 **D** matrix of the coefficients and the 6×1 column vector **A** of the weighting factors:

$$\begin{bmatrix} C_{13kl}\zeta_{kl}^{(1)} & \cdots & C_{13kl}\zeta_{kl}^{(6)} \\ \vdots & \ddots & \vdots \\ C_{33kl}\xi_{kl}^{(1)} & \cdots & C_{33kl}\xi_{kl}^{(6)} \end{bmatrix} \begin{bmatrix} A^{(1)} \\ \vdots \\ A^{(6)} \end{bmatrix} = \begin{bmatrix} 0 \\ \vdots \\ 0 \end{bmatrix}, \tag{9}$$

where $\zeta_{kl}^{(n)} = u_{k0}^{(n)} l_l^{(n)}$ and $\xi_{kl}^{(n)} = u_{k0}^{(n)} l_l^{(n)} \exp(-iql_3 d)$. The problem has nontrivial solutions when the determinant of matrix **D** is $|\mathbf{D}| = 0$. For the thin membranes, these solutions can be sorted with respect to the evaluated weighting factors $A^{(n)}$ and Eq. (5) in terms of the membrane mid-plane symmetry to corresponding Lamb waves, as shown in Table S2.

Table S2. Types of acoustic waves in membranes/plates.

Wave	Symbol	Symmetry relation
Symmetric Lamb	S	$u_3(-d) = -u_3(0)$
Antisymmetric Lamb	A	$u_3(-d) = u_3(0)$
Sher-Horizontal	SH	$u_3(-d) = u_3(0) = 0$

In the numerical approach, we swept v from 1 to 7000 m/s in Eq. (4) at a given q to find the minima of $|\mathbf{D}|$, which correspond to phase velocities of Lamb waves. This procedure is repeated for q varied from 0 to 25 µm^{-1} which corresponds to the range of wave numbers available in the BLS experiment. This approach allows plotting the dispersion relations $v(q)$ and $f(q)$.

S4.2. BLS spectra for bulk and membranes

Brillouin light scattering on acoustic phonons/waves originates from the surface ripple (SR) mechanism (or moving interface mechanism) and the photo-elastic (PE) mechanism. For the

acoustic waves polarized in the i-th direction and propagating in the free surface ($x_3 = 0$) BLS intensity can be calculated from the projected local density of states (PLDOS):

$$I_i = \langle |u_i(0)|^2 \rangle_{\mathbf{q},\omega} = \frac{k_\mathrm{B}T}{\pi\omega} \mathrm{Im}[G_{ii}(q,0,\omega)], \tag{10}$$

where $G_{ii}(q,0,\omega) = \sum_n A^{(n)} u_{i0}^{(n)}$ is the component of the Green's function tensor. The prefactor $k_\mathrm{B}T/\pi\omega$ is related to the thermal occupation of each phonon mode, where k_B is Boltzmann constant, T is temperature, and $\omega = 2\pi f$ is the angular frequency. For the surface ripple mechanism, BLS intensity is proportional to $\langle |u_3(0)|^2 \rangle_{q,\omega} \sim G_{33}$. Similarly, for the photo-elastic mechanism, the BLS intensity is proportional to the $\langle |u_1(0)|^2 \rangle_{q,\omega} \sim G_{11}$ and $\langle |u_2(0)|^2 \rangle_{q,\omega} \sim G_{22}$ for the bulk longitudinal and transverse waves, respectively. Next, G_{11} and G_{22} have to be scaled by the Ryeigh ratio $R^j \propto [e_\mathrm{s} T^j e_0]$ accounting for the photo-elastic coupling. Here, e_s, e_0 and T^j are unit vectors in the direction of the scattered and incident light polarization and the photo-elastic tensor, respectively.[10] For the [100] phonon in hexagonal crystal belonging to space group D_{6h}^4, PE tensors and velocities for longitudinal (L) and two transverse waves (T1, T2) are presented in Table S3.[10]

Table S3. Velocities and PE tensors for [100] phonon in MoSe$_2$. PE coefficients are denoted as p_{ij}, while ε_o and ε_e stand for ordinary and extraordinary dielectric constants, respectively. [10]

L	T1	T2
$v = (C_{11}/\rho)^{1/2}$	$v = (C_{66}/\rho)^{1/2}$	$v = (C_{44}/\rho)^{1/2}$
$T^\mathrm{L} = \begin{bmatrix} \varepsilon_o^2 p_{11} & 0 & 0 \\ 0 & \varepsilon_o^2 p_{12} & 0 \\ 0 & 0 & \varepsilon_o^2 p_{31} \end{bmatrix}$	$T^{\mathrm{T1}} = \begin{bmatrix} 0 & \varepsilon_o^2(p_{11}-p_{12})/2 & 0 \\ \varepsilon_o^2(p_{11}-p_{12})/2 & 0 & 0 \\ 0 & 0 & 0 \end{bmatrix}$	$T^{\mathrm{T2}} = \begin{bmatrix} 0 & 0 & \varepsilon_o\varepsilon_e p_{44} \\ 0 & 0 & 0 \\ \varepsilon_o\varepsilon_e p_{44} & 0 & 0 \end{bmatrix}$

In the backscattering BLS geometry, p-p and s-s polarizations correspond to $e_0 = e_\mathrm{s} = \begin{bmatrix} 1 & 0 & 0 \end{bmatrix}$ and $e_0 = e_\mathrm{s} = \begin{bmatrix} 0 & 1 & 0 \end{bmatrix}$, respectively. Thus, we obtain $[e_\mathrm{s} T^\mathrm{L} e_0] \neq 0$, $[e_\mathrm{s} T^{\mathrm{T1}} e_0] = 0$ and $[e_\mathrm{s} T^{\mathrm{T2}} e_0] = 0$. For the light polarized in the p-s configuration, we get $[e_\mathrm{s} T^\mathrm{L} e_0] = 0$, $[e_\mathrm{s} T^{\mathrm{T1}} e_0] \neq 0$ and $[e_\mathrm{s} T^{\mathrm{T2}} e_0] = 0$. Therefore, in our experiment T2 is BLS-inactive in any configurations of polarizations.
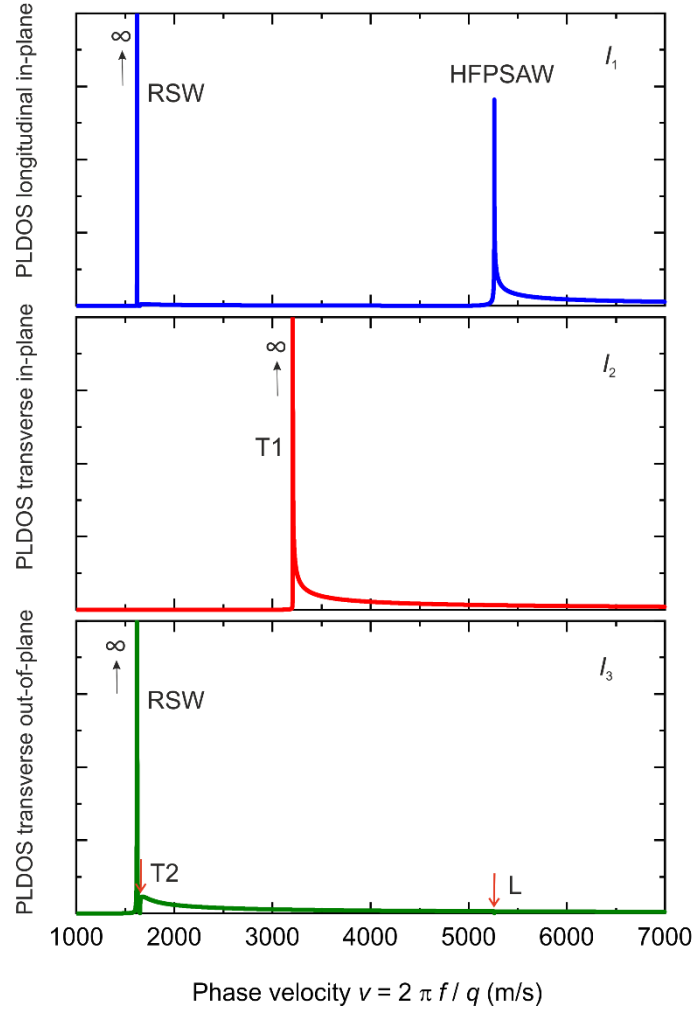
Figure S8. Projected local density of states (PLDOS) as a function of the acoustic wave phase velocity. Abbreviations: RSW – Rayleigh surface wave, HFPSAW – high frequency pseudo surface acoustic wave, L – longitudinal bulk wave, T1 – fast transverse wave, T2 – slow transverse wave.

Figure S8 displays PLDOS as a function of the phase velocity calculated using elastic constants of bulk $MoSe_2$. The out-of-plane component of PLDOS is BLS-active solely due to the SR effect, while the in-plane transverse and longitudinal solely due to the PE effect. RSW is associated with both longitudinal in-plane and transverse out-of-plane PLDOS. Thus, RSWs are BLS active due to the superposition of the SR and PE effects in the *p-p* polarization of the incident and scattered light. RSW satisfies the stress boundary condition, and hence the corresponding peak intensity tends to infinity. The out-of-plane PLDOS reveals the so-called Lamb shoulder above the T1 threshold. This surface-like band is a continuum of waves that originates in propagating bulk transverse and evanescent longitudinal waves. The Lamb shoulder can be considered as the continuum of high order (*m*>0) Lamb waves in a plate/membrane of infinite thickness. In such a case, the fundamental (*m*=0) symmetric and antisymmetric Lamb waves turn into RSW. In the case of the BLS spectra of bulk $MoSe_2$ [Fig. 2(b) in the main text] the dip located at T2 is overwhelmed by the

RSWs peak, and the Lamb shoulder is resolved as the high-frequency tail of the RSW peak. In the case of the SR scattering, the mode conversions effect leads to a sharp dip located at the L threshold. Notably, this dip coincides with a well-defined peak of HFPSAW in longitudinal in-plane PLDOS. HFPSAWs do not satisfy the stress-free boundary condition; thus, they are leaky (skimming) surface waves that radiate their energy into the bulk. This is reflected by the asymmetric peak broadening in BLS spectra. In the case of considered bulk MoSe$_2$, the velocity HFPSAWs is practically equal to the velocity of L BAW.[6]

The transverse in-plane component of PLDOS reveals the peak associated with the fast transverse T2 (shear-horizontal, SH) wave, which is BLS-active due to the PE effect in the *p-s* (or *s-p*) configuration. This wave satisfies the stress-free boundary condition, leading to the infinite peak intensity, as shown in Fig. S8. However, the T2 peak is associated with a high-frequency tail resolved in the experiment as asymmetric broadening. This tail can be described as a continuum of higher-order ($m>1$) SH modes propagating in a membrane/plate of infinite thickness. [11]

We involved such factors as finite optical aperture, instrumental broadening, and phonon attenuation in calculating the BLS spectra.[12] In general, this resulted in peak broadening and asymmetry. We note that the exact calculations of SR and PE contributions to BLS spectra of bulk and ultra-thin MoSe$_2$ were not possible due to a lack of relevant optical properties (PE tensor and full dielectric tensor).

S4.3. Membrane thickness and stress
To determine the thickness of membranes from the experimental dispersion of A0 mode, we repeated the procedure described in S4.1. where we swept d and σ^0 at fixed C_{ij} and ρ. Figure S9 (a) displays exemplary experimental dispersion of A0 mode compared with dispersion relations calculated for five thickness differing by 1L. This example illustrates that the change in d even by one layer has a notable influence on the calculated dispersion.

The calculated and experimental frequencies denoted as f_i^{c} and f_i^{e}, respectively, were compared for n wave numbers (experimental points) employing the reduced chi-square statistics for determining the goodness of the fit:

$$\chi^2 = \frac{1}{N}\sum_i^n \frac{(f_i^{\mathrm{c}} - f_i^{\mathrm{e}})^2}{(\Delta f^c)^2 + (\Delta f^e)^2},\qquad(11)$$

where Δf^c and Δf^e are errors for calculated and experimental frequency, respectively. The former was taken as the difference of calculated frequencies for limits of $C_{11} \pm \Delta C_{11}$, while the latter comes from the Lorentzian fit of the BLS peak. The degree of freedom, $N = n - m$, is determined as the difference between n and number of fitted parameters m = 2, except for membranes with $\sigma^0 = 0$ MPa for which m = 1. We calculated the χ^2 for a selected range of d and σ^0 and found χ^2_{min}. Figure S9 (b) displays the 95 % and 68.3 % confidence regions for

exemplary membrane (d = 5.2 nm) for which $\chi^2(d,\sigma^0) - \chi^2_{\min} < 5.991$ and $\chi^2(d,\sigma^0) - \chi^2_{\min} < 2.6$, respectively. In the case of membranes with $\sigma^0 = 0$ for which m = 1, 95 % and 68.3 % confidence regions are given by $\chi^2(d) - \chi^2_{\min} < 3.84$ and $\chi^2(d) - \chi^2_{\min} < 1$, respectively. The membrane thickness and stress with errors determined from confidence regions are listed in Table S4. In this way, we obtained thicknesses that are consistent with those measured by optical contrast. Overall, the uncertainty of the thickness obtained from BLS can be estimated as ±1 L.
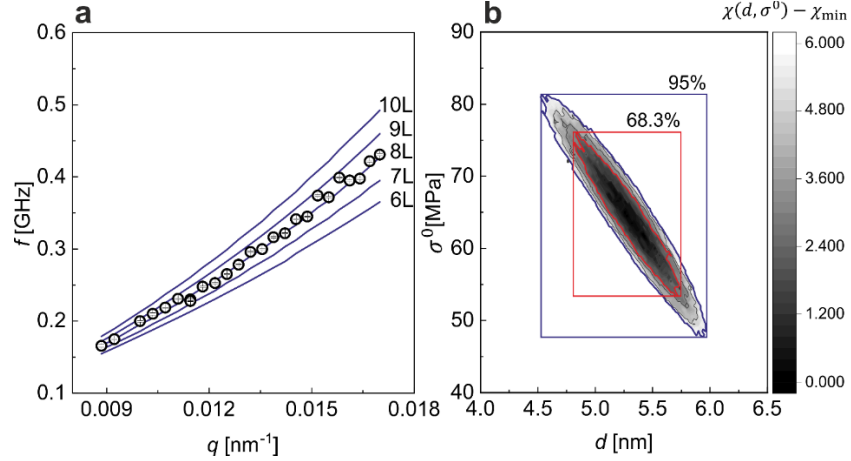

Figure S9. (a) Calculated (lines) dispersion relations for different MoSe$_2$ thicknesses given as a number of layers (L) and experimentally determined dispersion (circles). (b) 95% and 68.3% confidence regions for determining the d and σ^0 of exemplary (d=5.2 nm) MoSe$_2$ membrane.

Section S5. Raman spectroscopy

Raman spectroscopy measurements were performed with the incident light wavelength of 633 nm. Figure S10 (a) displays Raman spectra for all MoSe$_2$ membranes and the bulk sample. The captured peaks can be assigned to A$_{1g}$ mode. The E$_{1g}$ mode was not resolved since we used the lowest possible power (< 50 µW) to correctly resolve the A$_{1g}$ and avoid additional redshift due to the temperature rise (also thickness dependent) that could obscure the result.

The Raman shift of A$_{1g}$ mode as the function of the membrane thickness (determined by BLS) is plotted together with the literature data[13] in Fig. S10 (b). Notably, our results qualitatively follow the trend reported in the prior work. This behavior confirms the sorting of the membranes in terms of their thickness obtained from BLS. More quantitative analysis of the Raman data requires correction of the A$_{1g}$ spectral position with respect to a reference frequency from the literature data. The Raman data of bulk MoSe$_2$ in Ref. [13] was not reported. As the reference, we used the spectral position of the A$_{1g}$ measured for the sample, which thickness was determined by the optical contrast as 3L. In addition, we estimated the redshift due to the stress using the coefficient $\Delta\omega(A_{1g})/\varepsilon \cong -1$ for MoS$_2$ taken from the literature[14] (not available for MoSe$_2$). Here, ε denotes strain in % that can be calculated from Hooke's law and BLS results

(elastic tensor and stress). The effect of stress is relatively minor except for the sample of the highest stress (4.9 nm thick, 188 MPa).

To determine the thickness of the membranes from (corrected) Raman results, we first fitted the literature data with a function: $\omega(A_{1g}) = (ld + m)/(nd + o)$, where $l, m, n,$ and o are free fitting parameters. Using the fitted parameters, we estimated the thicknesses of our MoSe$_2$ membranes from the Raman shift of A$_{1g}$. The inset in Fig. S10 (b) shows the comparison of thicknesses determined by Raman and BLS.
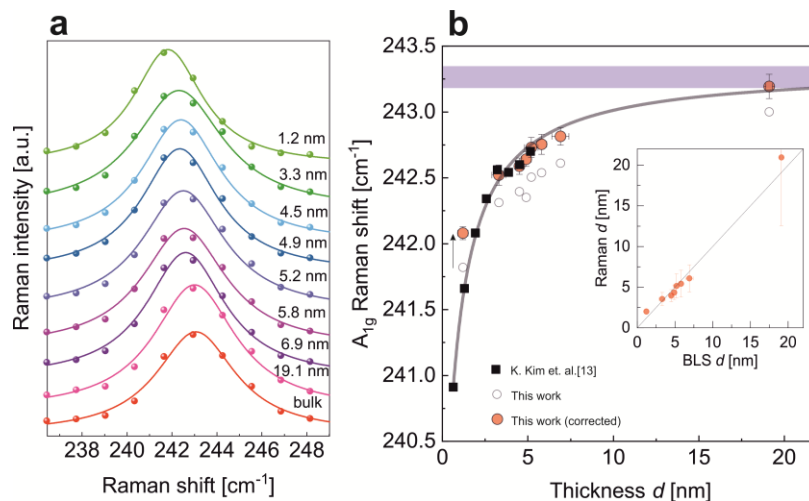

Figure S10. (a) Raman spectra of A$_{1g}$ mode for bulk MoSe$_2$ and membranes of different thicknesses determined by BLS. (b) Raman shift of A$_{1g}$ mode as a function of the membrane thickness. Squares stand for the experimental data from the literature.[13] Open circles stand for experimental data from this work. Solid circles represent experimental data after corrections (reference line, residual stress) described in the text. Shaded area corresponds to experimentally measured bulk value from this work. A solid line denotes the fit of literature data with the function described in the text. Inset in (b) shows the comparison of thicknesses determined by Raman and BLS.

Table S4 gathers the thicknesses for all the samples, determined by optical contrast, AFM, BLS, and Raman. Overall, all four techniques are complementary and in agreement, with AFM providing accurate values for thick samples and optical contrast for thinner ones, as discussed in Section S1. Importantly, BLS provides a broader range of applicability, from thin to thick samples.

Table S4. Thickness determined by various techniques and residual stress determined by BLS.

Optical contrast d (nm)	AFM d (nm)	BLS d (nm) 68.3% conf.	BLS d (nm) 95% conf.	Raman A_{1g} (cm^{-1})	Raman d (nm)	BLS σ^0 (MPa) 68.3% conf.	BLS σ^0 (MPa) 95% conf.
1.9 (3L)	NA	1.2±0.3	1.3±0.3	241.82±0.05	2.01±0.25	103±3	103±3
2.9±0.4 (4-5L)	6.3±1.9	3.3±0.4	3.3±0.6	242.31±0.08	3.5±0.8	27±8	27±14
4.2±0.4 (6-7L)	NA	4.5±0.1	4.5±0.2	242.40±0.07	3.9±0.7	0	0
4.5(7L)	6.7±1.5	4.9±0.3	4.9±0.4	242.35±0.06	4.35±0.5	188±6	188±9
5.2(8L)	5.1±1.6	5.2±0.4	5.2±0.7	242.51±0.08	5.15±1.5	65±11	65±17
5.5±0.4(8-9L)	5.2±1.2	5.8±0.3	5.8±0.4	242.54±0.08	5.4±1.6	46±7	46±10
NA	8.8±0.7	6.9±0.5	6.9±0.7	242.61±0.07	6.1±1.7	22±15	22±22
NA	24.7±1.3	19.1±0.2	19.1±0.5	243.0±0.1	21±8	0	0
bulk	/	/	/	243.07±0.09	/	/	/

Table S5. Elastic constant values of monolayer and bulk MoSe$_2$ found in the literature. Experimental and theoretical values are indicated with superscripts [e] and [t], respectively.

	C_{11} (GPa)	C_{12} (GPa)	C_{33} (GPa)	C_{44} (GPa)	C_{13} (GPa)	Ref.
Monolayer	171.3^t	39.7^t	/	/	/	[15]
	171.6^t	39.8^t	/	65.9^t	/	[16]
	165.7^t	39.7^t	/	/	/	[17]
	176.9^t	67.1^t	/	/	/	[17]
Bulk	196.10^t	42.30^t	44.70^t	32.90^t	9.80^t	[18]
	/	/	/	16.80^e	/	[19]
	179.81^t	40.75^t	35.49^t	15.90^t	8.46^t	[20]
	/	/	54.90^e	/	/	[4]
	/	/	/	18.70^e	/	[21]

Table S6. Experimentally determined elastic constants for selected vdW materials.

material	technique	C_{11} (GPa)	C_{12} (GPa)	C_{13} (GPa)	C_{33} (GPa)	C_{44} (GPa)	Ref.
graphite	Inelastic x-ray scattering	1109	139	0(3)	38.7	5.0	[22]
	Ultrasonic+sonic resonance+static test+BLS	1056	180	15	36.5	0.18- 5	[23–25]
	Neutron scattering	1440	520	/	37.1	4.6	[26]
MoS$_2$	Neutron scattering	238	-54	23	52	19	[27]
TaSe$_2$	Neutron scattering	229	107	/	54	18.5	[28]
NbSe$_2$	Neutron scattering	194	91	/	42	17.6	[28]
		171	79	-2	62	19	[27]
WS$_2$	Neutron scattering	150	/	/	60	16	[2]
MoSe$_2$	**BLS**	**191±3**	**49±4**	**/**	**/**	**18.8±0.7**	**This work**

Section S6. The dispersion of acoustic waves in MoSe$_2$ membranes.

Figure S11 displays Lamb waves dispersion relation obtained by the numerical approach for 6.9±0.5 nm thick MoSe$_2$. For comparison, we plotted the dispersions of longitudinal (L) and transverse (T2) bulk wave, calculated using C_{11} and C_{66}. Clearly, L and the fundamental symmetric Lamb wave (S0) [indicated by arrows] overlap within the available qd in BLS (shaded area). Also, the dispersion of the SH0 mode is identical to that of T2 bulk wave.
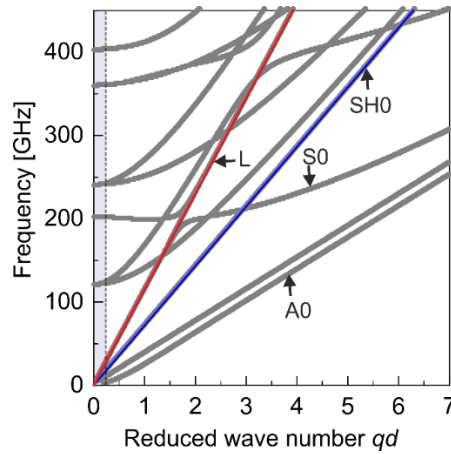

Figure S11. Calculated dispersion $f(qd)$ for 6.9 nm thick MoSe$_2$ membrane. Asymmetric (A0), symmetric Lamb (S0), and shear horizontal (SH0) as well as longitudinal wave (L), calculated from the experimentally determined C_{11}, are indicated with arrows. The shaded area shows the qd range available in BLS experiment.

Section S7. Influence of the elastic constants and the membrane thickness on the dispersion of the antisymmetric Lamb wave (A0)

In general, the dispersion relation of A0 mode depends on such parameters as C_{11}, C_{12}, C_{13}, $C_{33,}$ C_{44}, σ^0, d and ρ. When the mass density ρ is known, the residual stress σ^0 can be obtained independently from the cut-off velocity at $q = 0$.[12] To examine the impact of the remaining parameters on the A0 mode dispersion, we employed the numerical approach described in Section S4. For a given set of parameters, the resulting dispersion $f(q)$ was fitted using a simple formula $f = aq^2$. Figures S12 (a) and (b) display the relative change $\Delta a/a$ as a function of the relative change of elastic constants and the membrane thickness, respectively. Here, in the case of the elastic constants, the main effect comes from C_{11} while the others remain negligible. Notably, C_{11} is determined independently from the dispersion of the S0 mode. However, the main

impact comes from the membrane thickness, as evident in Fig. S12 (b). Consequently, the dispersion relation of the A0 mode can be used to determine the thickness of the membrane.
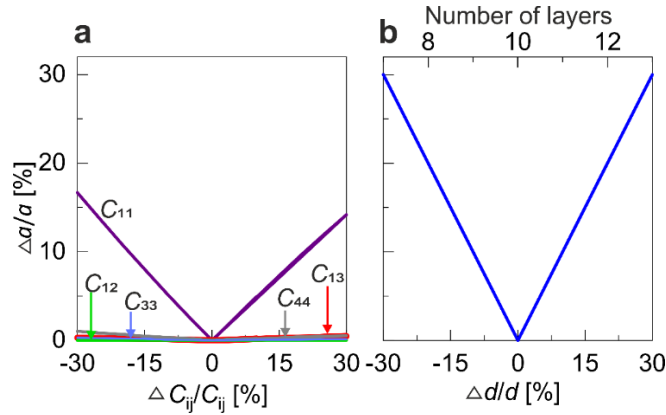

Figure S12. The impact of the relative change in (a) the elastic constants and (b) the membrane thickness on the dispersion of the A0 mode.

Table S7. Experimentally determined elastic constants and residual stress for bulk and freestanding MoSe$_2$ of various thicknesses by BLS. C_{33} and C_{13} are taken from the literature.

d (nm)	σ^0 (MPa)	C_{11} (GPa)	C_{12} (GPa)	C_{33} (GPa)[4]	C_{44} (GPa)	C_{13} (GPa)[18]
1.2±0.3	103±3	131±2	29±3	27.0		
3.3±0.4	27±8	150±3	34±4	49.0		
4.5±0.1	0	163±3	37±4	51.0		
4.9±0.3	188±6	158±2	36±3	52.0	18.8±0.7	9.8
5.2±0.4	65±11	164±3	40±4	52.0		
5.8±0.3	46±7	169±2	43±3	53.0		
6.9±0.5	22±15	171±3	39±4	53.0		
19.1±0.2	0	183±2	43±3	54.9		
Bulk	/	191±3	49±4	54.9		

Section S8. In-plane Young modulus

We calculate Young modulus as $E_{11} = 1/S_{11}$ where S_{11} is the element of the compliance matrix that is defined as the inverse of elastic tensor given by Eq. (2). The compliance matrix for a hexagonal crystal is given as:

$$S_{KL} = \begin{bmatrix} S_{11} & S_{12} & S_{13} & 0 & 0 & 0 \\ S_{12} & S_{11} & S_{13} & 0 & 0 & 0 \\ S_{13} & S_{13} & S_{33} & 0 & 0 & 0 \\ 0 & 0 & 0 & S_{44} & 0 & 0 \\ 0 & 0 & 0 & 0 & S_{44} & 0 \\ 0 & 0 & 0 & 0 & 0 & S_{66} \end{bmatrix} = C_{KL}^{-1} =$$

$$\frac{1}{|C_{KL}|}\begin{bmatrix} C_{11}C_{33} - C_{13}^2 & C_{13}^2 - C_{12}C_{33} & (C_{12} - C_{11})C_{13} & 0 & 0 & 0 \\ C_{13}^2 - C_{12}C_{33} & C_{11}C_{33} - C_{13}^2 & (C_{12} - C_{11})C_{13} & 0 & 0 & 0 \\ (C_{12} - C_{11})C_{13} & (C_{12} - C_{11})C_{13} & C_{11}^2 - C_{12}^2 & 0 & 0 & 0 \\ 0 & 0 & 0 & \frac{|C_{KL}|}{C_{44}} & 0 & 0 \\ 0 & 0 & 0 & 0 & \frac{|C_{KL}|}{C_{44}} & 0 \\ 0 & 0 & 0 & 0 & 0 & \frac{2|C_{KL}|}{C_{11}-C_{12}} \end{bmatrix}, \qquad (12)$$

where $|C_{KL}|=(C_{11} - C_{12})(C_{11}C_{33} + C_{12}C_{33} - 2C_{13}^2)$ is the determinant of C_{KL} given in Eq. (2)

Therefore, we calculate Young modulus from the formula: $E_{11} = (C_{11} - C_{12})(C_{11}C_{33} + C_{12}C_{33} - 2C_{13}^2)/(C_{11}C_{33} - C_{13}^2)$. As we can infer from Fig. S13, the main impact on the in-plane Young modulus comes from C_{11} and C_{12}. Notably, both constants were determined in this work.
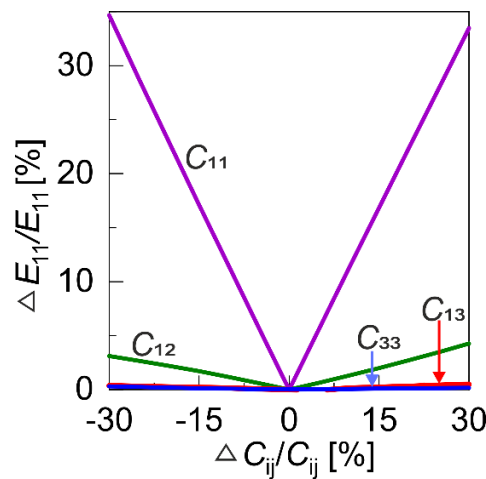

Figure S13. The impact of the relative change of C_{ij} on the in-plane Young modulus E_{11}.

Section S9. Young modulus of selected van der Waals materials

One of the most studied van der Waals (vdW) material is graphene. It is broadly accepted that 2D graphene features superior elastic properties in comparison to the corresponding bulk. However, the experimental values found in the literature are scattered, comparing values obtained by different techniques and different structures, like layers exfoliated from single crystal or kish graphite and carbon nanotubes. For example, the value of Young modulus (E) estimated from Raman measurements for single and bilayer graphene was 2.4±0.4 and 2.0±0.5 TPa, respectively,[29] being significantly larger than the bulk value of about 1 TPa.[22,24] However, some other experiments show that the E of the monolayer matches the bulk value, i.e., 1.05 ± 0.10 TPa by Raman[30] and 1.0±0.1 TPa by nanoindentation in atomic force microscope (AFM).[31] AFM measurement of graphene flakes of thickness between 2 and 8 nm, exfoliated from kish graphite, showed lower E about 0.5 TPa.[32] Young modulus of 5 and 8 nm thick graphene exfoliated from the natural crystal was determined to be 594 and 559 GPa, respectively, using the nonlinear dynamic response approach.[33] A very recent study measured E = 0.95±0.12 TPa for monolayer single-crystal graphene using a bulge test.[34] Moreover, a decrease of the in-plane E for monolayer graphene down to 60 GPa, attributed to the crumpling of the freestanding membrane, was observed.[35] Another recent study explored the effect of thickness on Young modulus for two vdW materials, namely graphene and boron nitride, by nanoindentation. On one side they found E = 1.026±0.022 TPa, and E = 0.942±0.003 TPa for 1L and 8L graphene, respectively. On the other hand, they found E values of 1L and 9L BN to be quite similar: 865±73 and 856±3 GPa, respectively.[36] For the case of MoS_2, the most studied member of TMDC, values of Young modulus measured by different techniques are scattered as well. To study whether the Young modulus of thin MoS_2 films changes compared to the bulk, we first need to establish its bulk value. Some authors compare Young modulus to elastic constant C_{11} = 238 GPa determined from neutron scattering data,[27] which can be misleading. From the elastic constants of bulk MoS_2 presented in the paper mentioned above, the in-plane Young modulus $E_{11} \sim 210$ GPa can be calculated.[27] Young modulus determined for 1L and 2L MoS_2 by nanoindentation was 270±100 GPa and 200±60 GPa, showing substantial errors, making it difficult to identify any size effect.[37] Another nanoindentation study revealed $E \sim 210$ GPa for monolayer, matching the bulk value.[38] Yet, another nanoindentation study gave E = 330±7 GPa for 5-25L for ultrathin MoS_2 flake, quite higher with respect to the bulk.[39] Additionally, nonlinear dynamic response approach, reported Young modulus in a range 300-315 GPa for 5 nm thick MoS_2.[33] All the values of Young modulus discussed here are sorted in the Table S8.

Table S8. Experimentally measured Young modulus of graphene, BN, and MoS_2.

Material	Thickness	Technique	E (GPa)	Ref.
Graphene	Bulk	Estimated from neutron and x-ray scattering results	~1000	[22,24]
	Monolayer	Raman	2400±400	[29]
		Raman	1050±100	[30]
		AFM nanoidentation	1000±100	[31]
		Interferometric profilometry	60 - 100	[35]
		Nanoidentation	1026±22	[36]
		Bulge test	950±120	[34]
	2L	Raman	2000±500	[29]
	8L	Nanoidentation	942±3	[36]
	2-8 nm	AFM	500	[32]
	5 nm	Nonlinear dynamic response	594±45	[33]
	8 nm	Nonlinear dynamic response	559±23	[33]
BN	Monolayer	Nanoidentation	865±73	[36]
	9L	Nanoidentation	856±3 GPa	[36]
MoS_2	Bulk	Estimated from neutron scattering results	~210	[27]
	Monolayer	Nanoidentation	270±100	[37]
		AFM nanoindentation	~210	[38]
	2L	Nanoidentation	200±60	[37]
	5-25L	Nanoidentation	330±7	[39]
	5 nm	Nonlinear dynamic response	300±18	[33]
	5 nm	Nonlinear dynamic response	315±23	[33]

References

[1]   X. Zhang, D. Sun, Y. Li, G.-H. Lee, X. Cui, D. Chenet, Y. You, T. F. Heinz, J. C. Hone, *ACS Appl. Mater. Interfaces* **2015**, *7*, 25923.

[2]   C. Sourisseau, M. Fouassier, M. Alba, A. Ghorayeb, O. Gorochov, *Materials Science and Engineering: B* **1989**, *3*, 119.

[3]   M. Grzeszczyk, K. Gołasa, M. Zinkiewicz, K. Nogajewski, M. R. Molas, M. Potemski, A. Wysmołek, A. Babiński, *2D Mater.* **2016**, *3*, 025010.

[4]   P. Soubelet, A. A. Reynoso, A. Fainstein, K. Nogajewski, M. Potemski, C. Faugeras, A. E. Bruchhausen, *Nanoscale* **2019**, *11*, 10446.

[5]   J. R. Sandercock, *Phys. Rev. Lett.* **1972**, *28*, 237.

[6]   P. Mutti, C. E. Bottani, G. Ghislotti, M. Beghi, G. A. D. Briggs, J. R. Sandercock, in *Advances in Acoustic Microscopy* (Ed.: A. Briggs), Springer US, Boston, MA, **1995**, pp. 249–300.

[7]   J. R. Sanderocock, *Solid State Communications* **1978**, *26*, 547.

[8]   V. V. Aleksandrov, M. V. Saphonov, V. R. Velasco, *Phys. Rev. B* **1994**, *50*, 7793.

[9]   V. Bortolani, F. Nizzoli, G. Santoro, *Phys. Rev. Lett.* **1978**, *41*, 39.

[10] F. T. Arecchi, E. O. Schulz-Dubois, Eds. , *Laser Handbook. Vol. 2: ...*, North-Holland Publ. Co, Amsterdam, **1972**.

[11] X. Zhang, M. H. Manghnani, A. G. Every, *Phys. Rev. B* **2000**, *62*, R2271.

[12] B. Graczykowski, M. Sledzinska, M. Placidi, D. Saleta Reig, M. Kasprzak, F. Alzina, C. M. Sotomayor Torres, *Nano Lett.* **2017**, *17*, 7647.

[13] K. Kim, J.-U. Lee, D. Nam, H. Cheong, *ACS Nano* **2016**, *10*, 8113.

[14] A. McCreary, R. Ghosh, M. Amani, J. Wang, K.-A. N. Duerloo, A. Sharma, K. Jarvis, E. J. Reed, A. M. Dongare, S. K. Banerjee, M. Terrones, R. R. Namburu, M. Dubey, *ACS Nano* **2016**, *10*, 3186.

[15] Y. Yang, X. Li, M. Wen, E. Hacopian, W. Chen, Y. Gong, J. Zhang, B. Li, W. Zhou, P. M. Ajayan, Q. Chen, T. Zhu, J. Lou, *Adv. Mater.* **2017**, *29*, 1604201.

[16] F. Zeng, W.-B. Zhang, B.-Y. Tang, *Chinese Phys. B* **2015**, *24*, 097103.

[17] A. Kandemir, H. Yapicioglu, A. Kinaci, T. Çağın, C. Sevik, *Nanotechnology* **2016**, *27*, 055703.

[18] C. K. Ghosh, D. Sarkar, M. K. Mitra, K. K. Chattopadhyay, *J. Phys. D: Appl. Phys.* **2013**, *46*, 395304.

[19] X. Zhang, Q.-H. Tan, J.-B. Wu, W. Shi, P.-H. Tan, *Nanoscale* **2016**, *8*, 6435.

[20] Y. Asadi, Z. Nourbakhsh, *Journal of Elec Materi* **2019**, *48*, 7977.

[21] T. Kuzuba, M. Ishii, *phys. stat. sol. (b)* **1989**, *155*, K13.

[22] A. Bosak, M. Krisch, M. Mohr, J. Maultzsch, C. Thomsen, *Phys. Rev. B* **2007**, *75*, 153408.

[23] E. J. Seldin, C. W. Nezbeda, *Journal of Applied Physics* **1970**, *41*, 3389.

[24] O. L. Blakslee, D. G. Proctor, E. J. Seldin, G. B. Spence, T. Weng, *Journal of Applied Physics* **1970**, *41*, 3373.

[25] M. Grimsditch, *J. Phys. C: Solid State Phys.* **1983**, *16*, L143.

[26] R. Nicklow, N. Wakabayashi, H. G. Smith, *Phys. Rev. B* **1972**, *5*, 4951.

[27] J. L. Feldman, *Journal of Physics and Chemistry of Solids* **1976**, *37*, 1141.

[28] D. E. Moncton, J. D. Axe, F. J. DiSalvo, *Phys. Rev. B* **1977**, *16*, 801.

[29] J.-U. Lee, D. Yoon, H. Cheong, *Nano Lett.* **2012**, *12*, 4444.

[30] D. Metten, F. Federspiel, M. Romeo, S. Berciaud, *Phys. Rev. Applied* **2014**, *2*, 054008.

[31] C. Lee, X. Wei, J. W. Kysar, J. Hone, *Science* **2008**, *321*, 385.

[32] I. W. Frank, D. M. Tanenbaum, A. M. van der Zande, P. L. McEuen, *J. Vac. Sci. Technol. B* **2007**, *25*, 2558.

[33] D. Davidovikj, F. Alijani, S. J. Cartamil-Bueno, H. S. J. van der Zant, M. Amabili, P. G. Steeneken, *Nat Commun* **2017**, *8*, 1253.

[34] J. W. Suk, Y. Hao, K. M. Liechti, R. S. Ruoff, *Chem. Mater.* **2020**, *32*, 6078.

[35] R. J. T. Nicholl, H. J. Conley, N. V. Lavrik, I. Vlassiouk, Y. S. Puzyrev, V. P. Sreenivas, S. T. Pantelides, K. I. Bolotin, *Nat Commun* **2015**, *6*, 8789.

[36] A. Falin, Q. Cai, E. J. G. Santos, D. Scullion, D. Qian, R. Zhang, Z. Yang, S. Huang, K. Watanabe, T. Taniguchi, M. R. Barnett, Y. Chen, R. S. Ruoff, L. H. Li, *Nat Commun* **2017**, *8*, 15815.

[37] S. Bertolazzi, J. Brivio, A. Kis, *ACS Nano* **2011**, *5*, 9703.

[38] R. C. Cooper, C. Lee, C. A. Marianetti, X. Wei, J. Hone, J. W. Kysar, *Phys. Rev. B* **2013**, *87*, 035423.

[39] A. Castellanos-Gomez, M. Poot, G. A. Steele, H. S. J. van der Zant, N. Agraït, G. Rubio-Bollinger, *Adv. Mater.* **2012**, *24*, 772.